The Japan Society
of Applied Physics

LETTER

Real-time optical-resolution photoacoustic endoscope

View the article online for updates and enhancements.

Real-time optical-resolution photoacoustic endoscope

Hui Sun[1,2], Wei Wang[1,2], Zixin Zhang[1,2], Li Wang[1,2], Wuyu Zhang[1,2], Kedi Xiong[1,2*], and Sihua Yang[1,2]

[1]The MOE Key Laboratory of Laser Life Science and Institute of Laser Life Science, College of Biophotonics, South China Normal University, Guangzhou, 510631 People's Republic of China
[2]Guangdong Provincial Key Laboratory of Laser Life Science, College of Biophotonics, South China Normal University, Guangzhou 510631, People's Republic of China

*E-mail: xiongkd2012@163.com

Currently, the reported endoscopic system cannot meet the necessary conditions for real-time and optical-resolution clinical application simultaneously. In this study, by utilizing a high-repetition-rate laser and optimizing the overall structure of the probe, a real-time optical-resolution photoacoustic endoscope was developed, which could image targets in real time while maintaining a relatively constant lateral resolution. The endoscopic system has a best-resolution of 19 μm and a real-time imaging speed of 25 Hz. Experimental results demonstrate that this approach will push the promotion and commercialization of photoacoustic endoscopic imaging in a variety of preclinical and clinical applications.
© 2021 The Japan Society of Applied Physics

Colorectal cancer is one of the most common malignant tumors in the world, and the increase in the incidence of colorectal cancer is related to the pathophysiological mechanism of the disease.[1] Clinical correlation between the tumor margin and the surrounding vascular structure provide diagnostic information for evaluating the staging or progression of the disease and guiding treatment.[2] In recent years, endoscopic technology has been widely used to detect colorectal cancer by providing intuitive tissue morphology and vascular network information.[3–8] Visible light endoscopes are usually used to visualize the rectal wall to diagnose various diseases. However, due to the lack of depth resolution information and limited vascular sensitivity, the changes of epithelial dysplasia in the early stage of cancer development cannot be clearly visualized.[9–11] Optical coherence tomography endoscopic imaging detects tissue with high resolution and high sensitivity. However, strong optical scattering in tissue result that, these high-resolution optical techniques image tissue less than 1 mm.[12–15] In addition, although ultrasonic endoscope provides a deeper depth of penetration, it is unable to identify dysplastic or early tumors as the low resolution and poor tissue contrast.[16–18]

Photoacoustic endoscope (PAE), which embodies PA imaging in miniature probes, provides imaging of internal organs with optical absorption contrast based on its strong spectral imaging ability and high penetration, and obtain structural and functional information by visualizing blood vessels.[19–26] However, the clinical development of PAE is greatly limited due to slow imaging speed and poor resolution. For conducting in vivo endoscopic imaging, some research groups developed a method to improve the resolution of the system by using optical-resolution PAE (OR-PAE), excited by a focused spot.[27,28] Such as, Wang et al. reported that the optical-resolution photoacoustic endomicroscopy in vivo had a lateral resolution of 10 μm, but the imaging frame rate is only 2–4 Hz.[27] Song et al. studied the in vivo photoacoustic/ultrasonic dual-modality endoscopy with a miniaturized full field-of-view catheter, which only achieved the imaging frame rate of 5 Hz.[28] Although these endoscopic systems achieve a high spatial resolution, the imaging speed has impeded the further clinical transformation. On the country, some research groups used a variety of techniques to improve the imaging speed, which reduced the lateral resolution, so it is difficult to clearly show the pathological changes of the vascular network of the colorectal wall.[29] Such as, Chen et al. reported the high speed integrated endoscopic photoacoustic and ultrasound imaging system which made great progress in imaging speed, achieving 50 fps, but the system resolution is 250 μm.[29]

In this paper, a real-time OR-PAE imaging system is developed by optimizing the structure of the integral probe and using a high-frequency laser. The PAE imaging system obtain the structure and depth information of the colorectal vascular network. The imaging speed of the imaging system can reach 25 Hz, and the imaging resolution achieves the best lateral resolution of 21 μm. In order to evaluate the performance of our colorectal imaging system, phantom experiment and in vivo rabbit colorectal imaging study were carried out in this work.

The schematic diagram of the real-time OR-PAE system is depicted in Fig. 1. As shown in Fig. 1(a), the laser beam is emitted by the 532 nm laser (mosquito X 532-2-V, Innolas) with a repetition frequency of 50 kHz and a pulse width of 12 ns, and then coupled into a single-mode fiber through a fiber coupler ((PAF2-7 A, Thorlabs). The 50 kHz external trigger signal is simultaneously used to trigger the laser and the DAQ system. The DAQ module mainly includes an amplifier and an acquisition card. The signals are amplified by 50 dB low noise amplifier (LNA-650, RF Bay) and then collected by a high-speed acquisition card (M4i.4450-x8, Spectrum) at a sampling rate of 250 MHz and stored in a computer. The motor control module drives rotating and stepper motors, respectively. The sequence program of the motor recorded in the Field Programmable Gate Array (FPGA) transmits control signals to the drivers that control the motor to achieve real-time speed and matching forward step. In the image processing, all PA data are collected and processed on PC using user-defined LABVIEW (National Instruments) and MATLAB (R2016a, Math Works, Natick, MA, USA) programs.

Figure 1(b) shows the timing of triggering the motor drive in FPGA. The step angle is set to 1.8°. When the speed is increased to 25 fps, the trigger pulse sent to the motor is 5 kHz, and the period is 2/25 of the original pulse. During the experiment, the trigger signal was set to 5 kHz and sent to the FPGA to control the motor to increase from 2 to 25 fps at a constant speed within 10 s. At the end of the experiment, the motor will gradually decelerate from 25 fps to a stop to make the motor rotate stably and extend the service life of the protection motor.
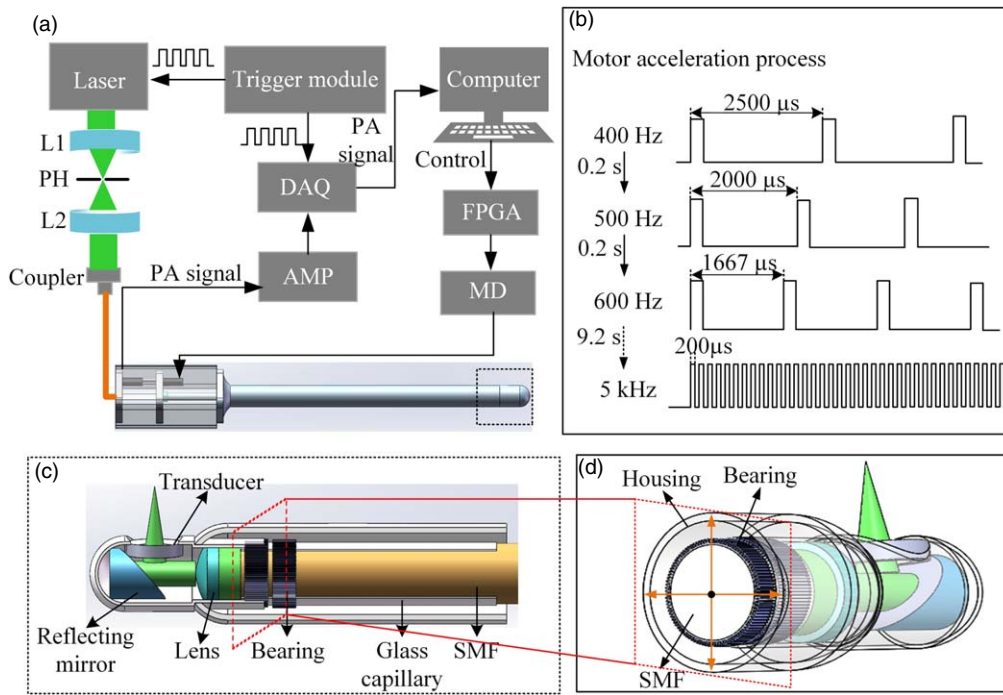
Fig. 1. (Color online) The schematic of real-time OR-PAE system. (a) PAE system. L1, L2, lens; PH, beam splitter; SMF, single mode fiber; DAQ, data acquisition system; AMP, amplifier; MD, motor driving. (b) The timing diagram of the real-time rotation of the motor. (c) Schematic diagram of the rotating forward and retractive structure of the probe. SMF, single mode fiber. (d) Another angle of view at the red dotted frame of (c).

As shown in the overall structure of the probe in Fig. 1(a), the probe adopts a cage structure with good stability and coaxiality. The built-in motor-based mechanical scanning mechanism enable easy integration of the optical and acoustical components and provide stable mechanical scanning, which ensures the coaxiality of the rotating shaft with the whole cage structure in the process of real-time rotation.

Figure 1(c) shows a schematic diagram of the internal structure of the probe. When the probe rotates, the laser beam

emitted from the optical fiber is focused on a lens with a focal length of 3 mm, and then reflected vertically from the glass column at an angle of 45° through the reflector. Figure 1(d) presents the different perspectives of Fig. 1(c). From this point of view, the outer diameter of the bearing and lens is the same as the inner diameter of the housing and can be stuck in the housing without falling off. The outer diameter of the glass capillary protecting the optical fiber is the same as the inner diameter of the bearing and is fixed with glue during
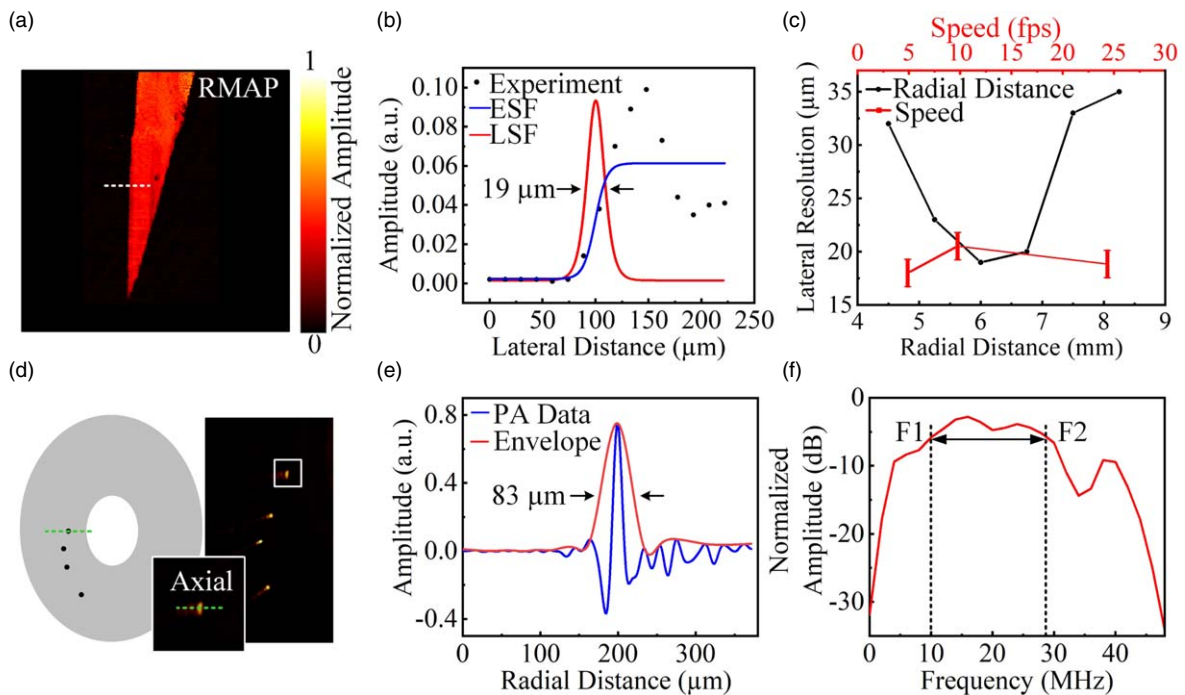

Fig. 2. (Color online) Evaluation of system performance. (a) RMAP PA image of blade formed. (b) Evaluation of the lateral resolution. The FWHM of the LSF derived from the ESF of the MAP image. (c) Lateral resolution of PA images at different depth and speed. (d) PA images of the 20 μm thick tungsten wire located at four locations. (e) Evaluation of the axial resolution. (h) Bandwidth of the transducer. F1, low frequency. F2, high frequency.

assembly. This design ensures that when the whole probe rotates and images, the optical path remains motionless and emits steadily, and there is a good coaxiality between these parts and the housing.

Figure 2 presents the performance of the probe. Figure 2(a) shows the radial-maximum amplitude projection (RMAP) image of the surgical blade. Figure 2(b) shows that the profile along the data point is fitted to obtain the edge spread function (ESF) curve, which is used to derive the line spread function (LSF) curve. The experimental lateral resolution of the system is about 19 μm. Figure 2(c) presents the bandwidth of the lateral resolution varying with depth and velocity, respectively. The lateral resolutions in the experiment are 18 μm, 21 μm and 19 μm respectively, which are calculated in the case of 5 fps, 10 fps and 25 fps, respectively. Figure 2(d) exhibits the experiment of axial resolution measurement. The picture on the left shows the arrangement of tungsten wire, and the picture on the right shows the B-scan imaging of tungsten wire by real-time photoacoustic probe. Figure 2(e) shows that the Gaussian fitting axial profile of the PA signal has a FWHM of ∼83 μm, which indicates the axial resolution of the system.

Figure 2(f) exhibits that the bandwidth (10–28.2 MHz@-6dB) of the ultrasonic transducer. F1 and F2 represent the low frequency and the high frequency respectively.

A phantom experiment of a leaf was conducted to evaluate the performance of the system. Figure 3(a) shows the schematic diagram of the experimental device. Two-hundred B-scans were obtained to recover a volume-rendered PA image at 5 fps, 10 fps and 25 fps, respectively. The acquisition time required for these three speeds is 40 s, 20 s and 8 s, separately. Figure 3(b) shows the B-scan of leaf veins at 5 fps, 10 fps and 25 fps, respectively. The B-scan images with different speeds are magnified to show the high resolution of the probe clearly. Figure 3(c) presents the RMAP of the leaf vein at 25 fps. The imaging range is from 0° to 360°, and the imaging length is about 3 mm. Figure 3(d) presents the SNR of photoacoustic images at three different frame rates. As can be seen from the curve in the picture, the optical resolution imaging with high signal-to-noise ratio can still be carried out while realizing real-time without much loss of signal-to-noise ratio. Figure 3(e) exhibits local RMAP of different rotational speed.
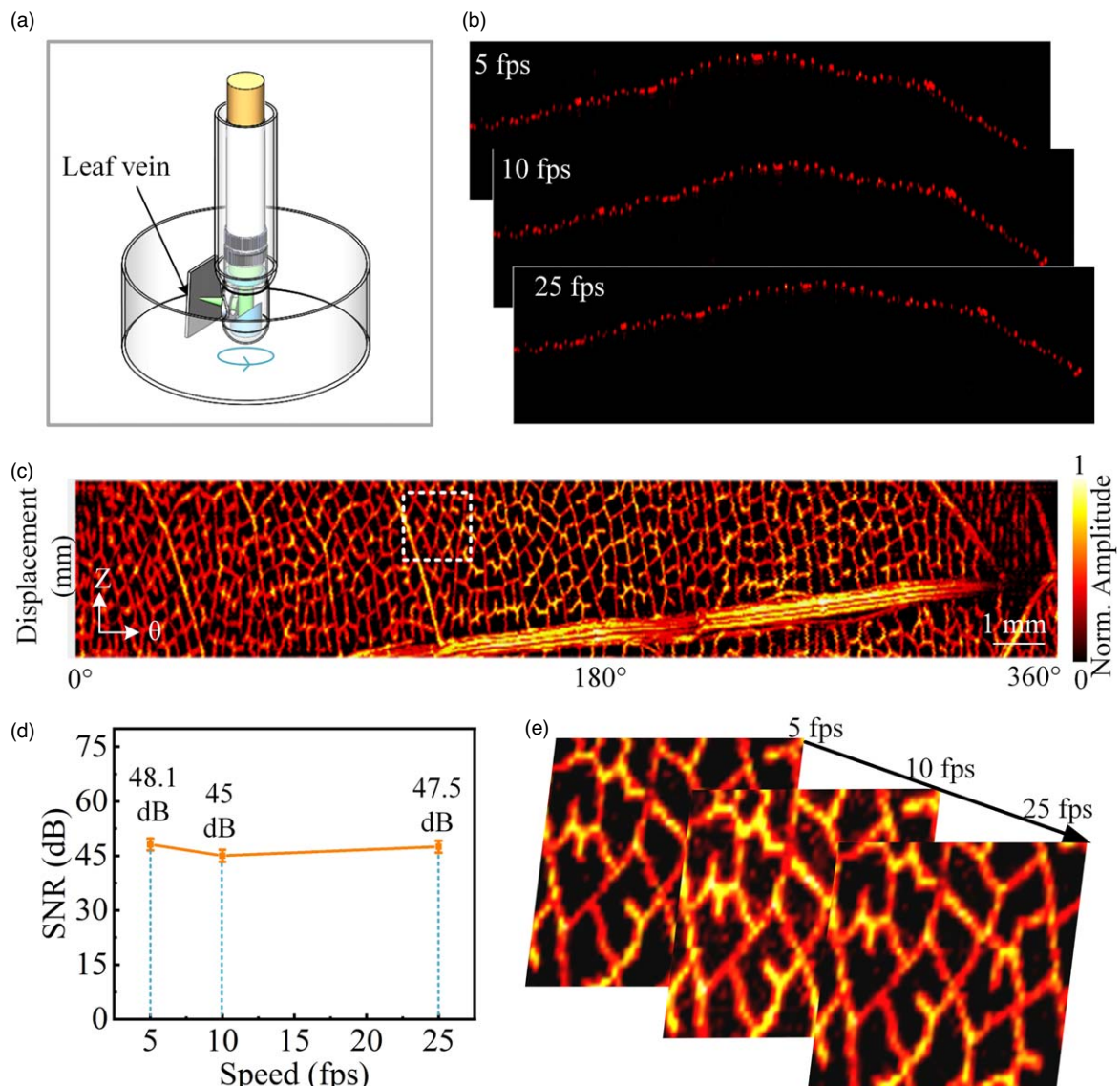

Fig. 3. (Color online) Imaging evaluation of the leaf phantom at different frame rates. (a) Schematic diagram of experimental device. (b) The B scan of leaf veins at 5 fps, 10 fps and 25 fps, respectively. (c) RMAP of leaf phantom at 25 fps. (d) The SNR of 5 fps, 10 fps and 25 fps, respectively. (e) Local RMAP of different rotational speed.
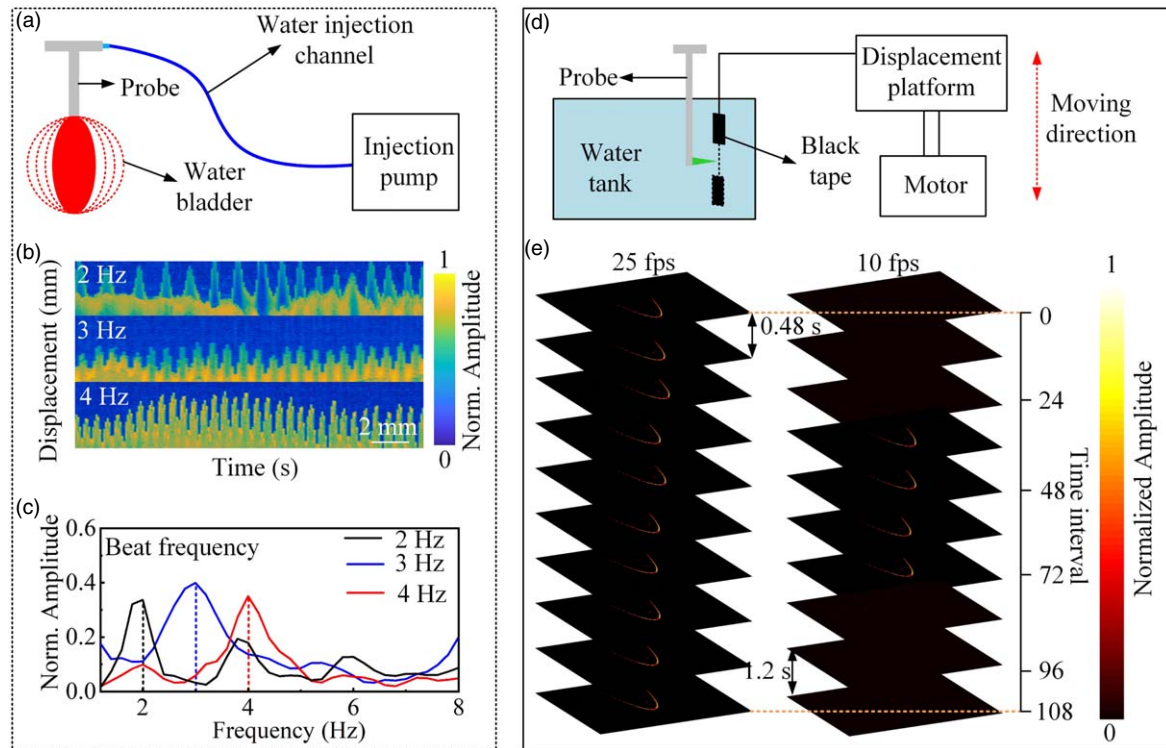
Fig. 4. (Color online) Dynamic signal capture experiment. (a) Schematic diagram of the device for (b). (b) The displacement at different frequencies of the water bladder. (c) Fourier transforms of the red line movements in (a) showing the frequencies. (d) Schematic diagram of the device for (e). (e) Capture of the same dynamic signal at 25 and 10 fps at the same B scan.

As shown in Fig. 4, in order to explore the role of real-time imaging of the system, two experiments of dynamic signal capture are designed. As shown in Fig. 4(a), the injection pump drives the syringe to inject and pump water, thus making the water bladder pulsate. Figure 4(b) shows that the time series of these cross-sectional images are arranged along the depth direction, and the displacement change image of the water bladder can be obtained. The displacement range of each image is 0 to 4.2 mm. In Fig. 4(c), Fourier analysis shows that the repetition frequency of the water bladder is about 2, 3, and 4 Hz, which are consistent with the actual fuel injection pump parameters. Figure 4(d) presents the motor was connected to a 5 mm long black tape and moved at a speed of 1 mm s^{-1}. Then the experimental results of this moving object are obtained by using 25 and 10 fps, as presented in Fig. 4(e). 125 B-scans are taken at the same position of the two imaging speeds, and extracted every 12 pieces, then a total of ten pictures are stacked. When the speed is 25 fps, the time interval is 0.48 s, and the time interval of 10 fps is 1.2 s. The vertical axis of the picture represents the number of time intervals. It can be seen that with the same number of pictures, the signal information captured by the probe in real-time imaging is 2.5 times more than that of low-speed imaging, such as 10 fps. The experimental results show the real-time OR-PAE has the potential to be used to monitor the respiratory rate and probe tracking of people or small animals under anesthesia.

To further demonstrate the feasibility of using the probe on biological tissues, we imaged the rectum of a New Zealand white rabbit (3 kg, female). In the experiment, the laser pulse energy in the tissue is within the safety limit of the American National Standards Institute (20 mJ cm^{-2}).[30] All procedures in the experiment were approved by the South China Normal University.

Figure 5 shows the results of real-time living imaging. Figure 5(a) shows the RMAP image of the rabbit rectal vascular network. The scanning time of 200 B-scan images is about 8 s, and the longitudinal length is 3 mm. Figure 5(b) shows the 3D imaging of blood vessels. The depth-coded image in Fig. 5(c) shows blood vessels at different depths. After the image is binarized by the threshold, the SEBOL operator is used to detect the edge of the binary image to obtain the vascular skeleton image, as shown in Fig. 5(d). Figure 5(e) presents a quantitative statistical diagram of the blood vessels diameter. There are two points of intersection between the straight line and the vascular skeleton. The distance between the two intersections is the diameter of the blood vessel. Finally, the diameter image of each point in the blood vessel is displayed in the form of a two-dimensional plan. As shown in Fig. 5(a), the diameters of blood vessels calculated by this method at D1, D2 and D3 are 200 μm, 60 μm and 20 μm, respectively. Figure 5(f) exhibits two B-scan images of in vivo experiment. The local magnifications of two B-scan images in the dotted frame show the good imaging resolution of the probe.

Here, we provide a real-time OR-PAE for colorectal vasculature information. The comparison between real-time and other frame rate leaf pulse experiments shows that the probe could ensure a good resolution while realizing real-time, and will not affect the sensitivity and spot quality of the probe. The experimental results of the dynamic information capture experiment show that in the real-time state, the capture of dynamic information is more accurate. The results obtained from the in-vivo New Zealand white rabbit experiment demonstrated that vasculature is identified by this integrated imaging system. While our PA imaging system has laid the groundwork for clinical imaging, several
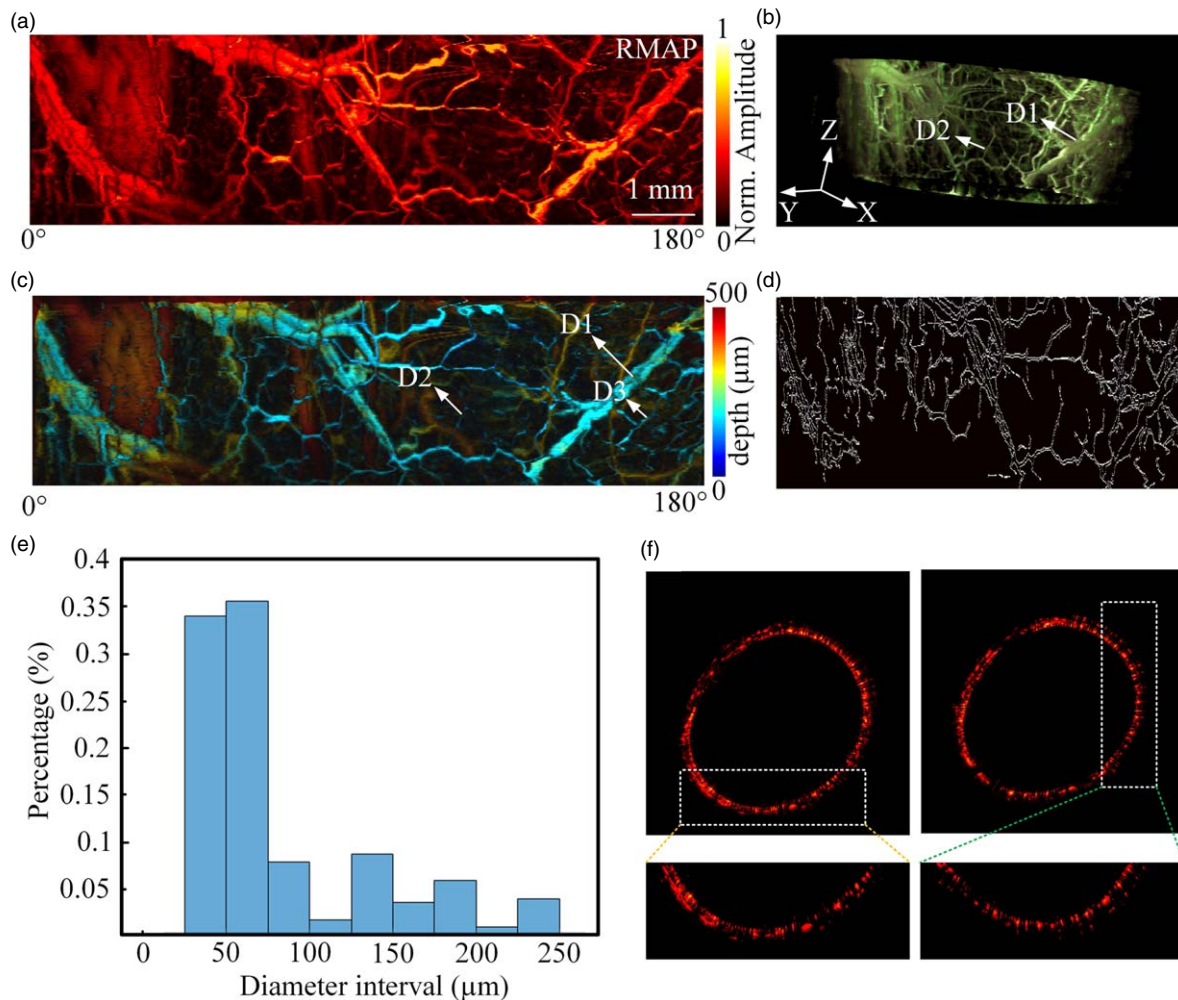
Fig. 5. (Color online) In vivo PA imaging of colorectum. (a) RMAP PA images of vascular network. (b) Three-dimensional PA images of rabbit rectum. (c) The depth-coded image of the blood vessels in the colorectal wall. (d) The vascular skeleton image. (e) Statistical chart of quantification of blood vessel diameter. (f) Two B-scan images of experiment.

challenges still need to be addressed for clinical integration. (1) The typical layered architecture: to distinguish the typical layered structure of the intestinal wall, ultrasonic imaging is needed in the imaging system, which could be achieved by using higher frequency acoustic transducers. (2) Probe size: for deeper and longer gastrointestinal imaging (such as rabbit or mouse esophagus), the diameter of the imaging probe is further reduced to ensure smooth insertion. This will be done by using smaller part sizes and fiber optics.

1) S. McGuire, Adv. Nutr. **7**, 418 (2016).
2) K. Xiong, W. Wang, T. Guo, Z. Yuan, and S. Yang, Opt. Lett. **44**, 2681 (2019).
3) B. Wang, C. Wang, F. Zhong, W. Pang, and J. Xiao, Quant. Imaging Med. Surg. **11**, 685 (2021).
4) S. Tang, J. Chen, P. Samant, K. Stratton, and L. Xiang, IEEE Trans. Med. Imaging **35**, 1780 (2016).
5) J. M. Yeh, C. Hur, Z. Ward, D. Schrag, and S. J. Goldie, Gut **65**, 563 (2016).
6) H. Wang, Y. Ma, H. Yang, H. Jiang, and H. Xie, Micromachines **11**, 928 (2020).
7) S. Zhang, R. Cheng, C. Tao, and X. Liu, Appl. Phys. Express **9**, 047301 (2016).
8) Z. Liu, C. Tao, and X. Liu, Appl. Phys. Express **12**, 057001 (2019).
9) C. Scheepers, Endoscopy **33**, 348 (2001).
10) B. Mayinger, F. Neumann, C. Kastner, T. Haider, and D. Schwab, Endoscopy **42**, 28 (2010).
11) H. Yanai, H. Nakamura, and K. Okita, Gastrointest. Endosc. **59**, P145 (2004).
12) N. Feucht, M. Maier, G. Lepennetier, M. Pettenkofer, C. Wetzlmair, T. Daltrozzo, P. Scherm, C. Zimmer, M. M. Hoshi, and B. Hemmer, Mult. Scler. J. **25**, 224 (2019).
13) J. Wang, Y. Hu, and J. Wu, Appl. Opt. **57**, 10056 (2018).
14) O. Nadiarnykh, N. A. McNeill-Badalova, M. Gaillard, M. I. Bosscha, and A. C. Moll, Acta Ophthalmol. **982**, 158 (2020).
15) H. Wang, C. P. Fleming, and A. M. Rollins, Opt. Express **15**, 3085 (2019).
16) Z. Turani, E. Fatemizadeh, T. Blumetti, S. Daveluy, and A. F. Moraes, Cancer Res. **79**, 2021 (2019).
17) X. Yuan, Y. Wang, J. Yuan, Q. Cheng, X. Wang, and P. L. Carson, Ultrasonics **91**, 1 (2018).
18) D. P. Darrow, Neurotherapeutics **16**, 88 (2019).
19) H. Jin, Z. Zheng, S. Liu, and Y. Zheng, IEEE Trans. Med. Imaging **39**, 1 (2020).
20) J. Tian, H. Guo, H. Jiang, B. Ke, and L. Xi, Opt. Lett. **42**, 4434 (2017).
21) X. Bai, X. Gong, W. Hau, R. Lin, J. Zheng, C. Liu, C. Zeng, Z. Xin, H. Zheng, and S. Liang, PLoS One **9**, e92463 (2014).
22) H. Guo, C. Song, H. Xie, and L. Xi, Opt. Lett. **42**, 4615 (2017).
23) L. Xi, C. Duan, H. Xie, and H. Jiang, Appl. Opt. **52**, 1928 (2013).
24) C. Miranda, E. Marschall, B. Browning, and B. S. Smith, Photoacoustics **19**, 100167 (2020).
25) X. Li, K. Xiong, and S. Yang, Appl. Phys. Lett. **114**, 163703 (2019).
26) K. Xiong, S. Yang, X. Li, and D. Xing, Opt. Lett. **43**, 1846 (2018).

27) J. M. Yang, C. Li, R. Chen, B. Rao, and L. V. Wang, Biomed. Opt. Express **6**, 918 (2015).

28) L. Yan, R. Lin, C. Liu, J. Chen, H. Liu, R. Zheng, X. Gong, and L. Song, J. Biophotonics **11**, e201800034 (2018).

29) Y. Li et al., IEEE J. Sel. Top. Quantum Electron. **25**, 7102005 (2019).

30) Laser Institute of America, *American National Standard for Safe Use of Lasers ANSI Z136.1–2014* (American National Stan dards Institute, Inc., Washington, DC, 2014).